

A THREE-DIMENSIONAL GRAPHICS APPLICATION FOR NUMERICAL SIMULATIONS OF TURBIDITY CURRENTS IN THE STRATIGRAPHIC MODELLING PROCESS

Fabio P. Figueiredo^a, Luiz Fernando Martha^b and David Waltham^c

^a*Tecgraf/PUC-Rio - Computer Graphics Technology Group, Pontifical Catholic University of Rio de Janeiro, Rua Marques de São Vicente, 225, Gávea, Brazil, fabiopf@tecgraf.puc-rio.br, <http://www.tecgraf.puc-rio.br/~fabiopf>*

^b*Civil Engineering Department and Tecgraf/PUC-Rio - Computer Graphics Technology Group, Pontifical Catholic University of Rio de Janeiro, Rua Marques de São Vicente, 225, Gávea, Brazil, lfm@tecgraf.puc-rio.br, <http://www.tecgraf.puc-rio.br/~lfm>*

^c*Department of Earth Sciences, Royal Holloway, University of London, Egham, Surrey TW20 0EX, England, d.waltham@es.rhul.ac.uk, <http://www.rhul.ac.uk/Earth-Sciences>*

Keywords: Turbidity currents, gravitational flows, numeric simulations, fluid dynamics, software, object-oriented programming, C++.

Abstract. Turbidity currents occur in both natural and man-made situations. In agreement with some researchers, most of the world's oil reserves are stored in hydrocarbon reservoir built by turbidity systems. Due to the importance of these currents, this work presents a three-dimensional graphics application for numerical simulations of turbidity currents called Turb3D. This application is based on a consistent and efficient numerical method for simulations of turbidity currents for basin sedimentations predictions in the stratigraphic modelling process. The algorithm used in the software is based on Navier-Stokes equations that are solved using a depth-averaged procedure. The application user interface provides a common, user-friendly, graphical environment for pre-processing, solution and post-processing. Despite the good computational performance achieved by using this approach, experiments should be done in order to validate the proposed numerical method presented in this work.

1 INTRODUCTION

Among the types of transport available in nature, water is by far the most important transport mechanism. However, this work will concentrate on the behaviour of a different transport mechanism: density currents. The main difference between these two mechanisms is that water transports individual sediment particles, or pieces of rocks, by dragging, saltation or suspension, while density currents consist of a sediment-fluid mixture that is under the influence of gravity, which explains the denomination gravity current.

Density current or gravity current occurs in both natural and man-made situations. Turbidity currents, debris flows, avalanches, oceanic fronts, pyroclastic flows and lava flows are some examples of this type of current.

Gravity currents are gravitational flows that move according to gravitational forces. The density difference between both fluids can be caused by thermal effects, dissolved or suspended material into the current, or by a combination of these two factors. The current is called conservative if the material is dissolved into the current. However, if the material is suspended it is called non-conservative.

Gravity currents have been discussed in many scientific studies, especially in geology. Their importance is due to the fact that these currents have a substantial influence on the deep-water depositional system. However, density currents can occur not only in submarine environments but also in subaerial environments.

To generate turbidity currents in a submarine environment, it is indispensable to have a solution of sediment and water mixture, which has normally a greater density than the surrounding water. The difference in density between two fluids is the ignition of gravity currents in general. A difference of only a few percent is enough to raise the fluid pressure force that together with the fluid weight component (if on a slope), induce the current to propagate. Based on the Reynolds number, it is possible to say that this propagation over time, velocity, might affect proportionally the flow turbulence (Waltham, 2004).

There has been extensive research on theoretical and experimental gravity currents. These studies have been conducted by many researchers from different areas with the objective of understanding the dynamics of these currents.

Mathematical modelling of gravity currents can provide significant insights into current velocity and thickness used to predict turbidite geometries and grain size distribution. Mathematical models range of forms from simple hydraulic equations and box models to highly complex turbulence models. In particular, mathematical models for gravity currents can be divided into four groups: simple model based on Chézy's equation, box models, depth-averaged models, and models incorporating turbulence.

The mathematical model used in this work was based on a depth-averaged approach. This approach was chosen because it is not as simple as Chézy's equation and it is not as complex as models incorporating turbulence, which require more CPU resources. Despite depth-averaged models unable to model fluid dynamic processes

within turbidity currents, this choice is arguably the best solution; as it produces relatively accurate predictions of current evolution and deposition with less demand on CPU resources.

2 MATHEMATICAL MODEL

2.1 General Gravity Flow Equations

The starting equations are (Acheson, 1990) the conservation of mass for an incompressible fluid given by

$$\sum_{i=1}^3 \frac{\partial u_i}{\partial x_i} = 0 \quad (1)$$

where u_i is velocity in the x_i -direction, and the conservation of momentum (Cauchy's equations of motion) given by

$$\frac{\partial u_j}{\partial t} + \sum_{i=1}^3 u_i \frac{\partial u_j}{\partial x_i} = T_j' + g_j \quad (2)$$

where j is 1, 2 or 3; t is time; g_j is gravity and

$$T_j' = \frac{1}{\rho} \sum_{i=1}^3 \frac{\partial T_{ij}}{\partial x_i} \quad (3)$$

with T_{ij} is stress in the i -direction on the plane perpendicular to the j -direction.

With depth-averaged equations we will only be interested in $j=1$ or 2 assuming $j=3$ corresponds to the vertical direction. This removes the gravity term from the right hand side of Eq. (2). Integrating Eq. (1) and (2) over the flow depth, h , and using Leibniz's theorem (Abramowitz & Stegun, 1964) then produces:

$$\sum_{i=1}^2 \frac{\partial}{\partial x_i} (h \bar{u}_i) + \frac{\partial h}{\partial t} = 0 \quad (4)$$

And

$$\frac{\partial}{\partial t} (h \bar{u}_j) + \sum_{i=1}^2 \frac{\partial}{\partial x_i} (h \bar{u}_i \bar{u}_j) = h \bar{T}_j' \quad (5)$$

where an overbar indicates a depth-averaged quantity. Finally, combining Eq. (4) and (5) gives:

$$\frac{\partial}{\partial t} (\bar{u}_j) + \sum_{i=1}^2 \bar{u}_i \frac{\partial}{\partial x_i} (\bar{u}_j) = \bar{T}_j' \quad (6)$$

which is simply a 2D version of Eq. (2). Eq. (4) and (6) are used to model the evolution of flow thickness and flow velocity respectively. These expressions are quite general

as they make no assumptions concerning rheological properties (e.g. non-zero viscosity or yield strength), flow style (e.g. laminar, turbulent or granular) or about how flow density varies in time and space. These factors only enter via the stress term on the right hand side of equation (6).

2.2 Stresses in a Turbulent Newtonian Flow

A Newtonian fluid is defined by the stress relationship (Acheson, 1990)

$$T_{ij} = -p\delta_{ij} + \mu \left(\frac{\partial u_j}{\partial x_i} + \frac{\partial u_i}{\partial x_j} \right) \quad (7)$$

where p is pressure and μ is viscosity. For the turbulent flow case considered in this paper, velocities should be understood as being ensemble averages (i.e. averages over a large numbers of identical flows) whilst μ is the eddy viscosity. For the low-concentration turbidity current case the flow density is nearly constant (i.e. equal to water density, ρ_w) so that Eq. (3) and (7) yield

$$\bar{T}_j \approx \frac{1}{\rho} \left(\frac{\partial \bar{p}}{\partial x_j} + \mu \overline{\nabla^2 u_j} + \tau_j(h) - \tau_j(0) \right) \quad (8)$$

where $\nabla^2 = \partial^2/\partial x_1^2 + \partial^2/\partial x_2^2$ and $\tau_j = \mu \partial u_j/\partial x_3$ is horizontal shear stress in the j direction.

For a thin flow, in which characteristic horizontal scales are generally much greater than flow thickness, a hydrostatic approximation is appropriate for calculation of the pressure gradient in Eq.(8). In addition, for simplicity, we assume that flow concentration is constant so that

$$\frac{\partial \bar{P}}{\partial x_j} = \frac{\partial P}{\partial x_j} = \Delta\rho g \frac{\partial h_f}{\partial x_j} \quad (9)$$

where $\Delta\rho$ is the density contrast between the flow and the ambient fluid and h_f is the height of the flow top.

The eddy-viscosity term in Eq. (8) is formally equivalent to a velocity-diffusion equation and this therefore simply smoothes the resulting velocity field. The diffusion coefficient is given by μ/ρ_w which depends upon the flow speed and could be anisotropic. However, for simplicity, we treat this as a constant modelling parameter chosen to ensure numerical stability.

The horizontal shear stress terms in Eq. (8) can be estimated using mixing-length theories (Duncan et al, 1960). We can approximate the relatively small contribution to shear-stress from the flow top by using a multiplier with the basal shear stress. The next step is to represent the basal stress by an equivalent shearing velocity, u_* , given by:

$$\tau = -\rho u_*^2 \approx -\rho_w u_*^2 \quad (10)$$

in which the negative sign indicates that stress acts in the opposite direction to the velocity. Within the turbulent boundary layer, the shearing velocity is related to the flow velocity by the law of the wall

$$u = \frac{u_*}{k} \ln\left(\frac{z}{z_0}\right) \quad z_0 < z < z_b \quad (11)$$

where k is von Kármán's constant (NB the clear-water value of ~ 0.41 is unlikely to be greatly in error for the low-concentration flows considered in this paper), z is height above channel floor whilst z_0 and z_b define the depth range of the turbulent boundary layer. Integration of Eq. (11) yields an average velocity over this boundary layer of

$$\bar{u}_b = \frac{u_*}{k} \left[\ln\left(\frac{z_b}{z_0}\right) - 1 + \frac{z_0}{z_b} \right] \approx \frac{u_*}{k} \left[\ln\left(\frac{z_b}{z_0}\right) - 1 \right] \quad (12)$$

assuming $z_b \gg z_0$. Above this boundary layer Kneller et al. (1999) showed experimentally that the velocity profile approximates well to a cumulative Gaussian function. However, for greater generality as well as mathematical simplicity, the average velocity in the upper part of the flow can be represented by the velocity at the top of the boundary layer multiplied by a constant, i.e.

$$\bar{u}_t = a u(z_b) = \frac{a u_*}{k} \ln\left(\frac{z_b}{z_0}\right) \quad (13)$$

where \bar{u}_t is the average velocity in the upper part of the flow and a is of order one.

Combining Eq. (12) and (13) then gives a depth-averaged velocity through the entire flow of

$$\begin{aligned} \bar{u} &= f \bar{u}_b + (1-f) \bar{u}_t \\ \bar{u} &= \frac{u_*}{k} \left[(f + (1-f)a) \ln\left(\frac{z_b}{z_0}\right) - f \right] \\ \bar{u} &= \frac{u_*}{k} b \ln\left(\frac{z_b}{z_0}\right) = \frac{u_*}{k} b \ln\left(\frac{hf}{z_0}\right) \end{aligned} \quad (14)$$

where $f = z_b/h$ is the fractional height of the boundary layer and $b = f + (1-f)a$ is a new constant of order one. Eq. (10) and (14) then combine to give

$$\tau = -\rho \left(\frac{k \bar{u}}{b \ln\left(\frac{hf}{z_0}\right)} \right)^2 \quad (15)$$

which, for the 2D (after depth-averaging) flows used here, may be generalized to

$$\tau_j = -\rho \bar{u}_j V \left(\frac{k}{b \ln\left(\frac{hf}{z_0}\right)} \right)^2 \quad (16)$$

where V is the depth averaged speed (i.e. $V^2 = \bar{u}_1^2 + \bar{u}_2^2$). Thus, the basal friction is

controlled by two constants; b which we assume is unity and z_0/f , which we show below to be closely related to the seafloor roughness. Note that this approach to calculating basal shear stress is formally equivalent to using a Chezy-type friction law except that the resulting Chezy-coefficient has a weak dependency on flow thickness and, more importantly, it is directly related to a potentially quantifiable parameter (i.e. the seafloor roughness).

The depth-averaged gravity current modelling algorithm described above has been validated by comparison with flume-tank experiments (Bitton et al, 2007).

2.3 Particulate Current Modifications

The preceding algorithm applies to any thin, turbulent gravity underflow and so, to complete the description, we need to add processes specifically related to sediment suspension and deposition. Our modelling is concerned with deposition from the distal parts of the flow so we assume the flow is fully developed in terms of sediment and ambient-fluid entrainment and that sediment deposition is therefore the dominant process.

For sediment suspension, the turbulence-generated root-mean-square fluctuations in vertical velocity should exceed the fall velocity, v_k (where k runs over all grain diameters), (Raudkivi 1998 but see Leeder et al. 2005 for a critique) and laboratory studies (e.g. Bagnold 1966; Kneller et al. 1999) show that the rms fluctuations are of similar magnitude to the shearing velocity. An entirely equivalent suspension criterion is that the Rouse number should be less than 2.5 (Rouse, 1937; Allen, 1997) since this also leads to the expectation of a suspension threshold when fall-velocity approximately equals the shear velocity. The sedimentation rate, s_k , is therefore zero for $u_* > v_k$ but equal to $c_k v_k$ (where c_k is concentration of the grain size) when the flow is stationary. The simplest mathematical model consistent with these end-members is

$$\begin{aligned} s_k &= c_k(v_k - u_*) & u_* &\leq v_k \\ s_k &= 0 & u_* &> v_k \end{aligned} \quad (17)$$

The still-water fall velocity can be calculated using a large number of different formulae but, for the first order model described in this paper, Stokes's Law is adequate. Each grain diameter is then independently modelled using a modified form of Eq. (4) which incorporates sediment loss:

$$\sum_{i=1}^2 \frac{\partial}{\partial x_i} (L_k \bar{u}_i) + \frac{\partial L_k}{\partial t} = -s_k \quad (18)$$

where L_k is the sediment load associated with grain-size k , i.e.

$$L_k = c_k h \quad (19)$$

Flow thickness is then recalculated using

$$h = c \sum_k L_k \quad (20)$$

where the total concentration of suspended sediments is assumed to be fixed for consistency with earlier model assumptions. Note that, as a consequence, flows thin as they loose sediment rather than become less concentrated.

3 COMPUTATIONAL MODEL

This Section shows the approach used for implementation of the governing equations presented in the previous section.

3.1 Governing equations solution

The summarised mathematical equations for turbidity current proposed in this work are given by the following expressions.

$$\frac{\partial h}{\partial t} + \frac{\partial}{\partial x}(h\bar{u}) + \frac{\partial}{\partial y}(h\bar{v}) = -\frac{S_k}{c_k} \quad (21)$$

$$\frac{\partial \bar{u}}{\partial t} + \frac{\partial}{\partial x}(\bar{u}^2) + \frac{\partial}{\partial y}(\bar{u}\bar{v}) = -\frac{1}{\rho} \left[\Delta\rho g \frac{\partial H}{\partial x} + \rho\bar{u}\sqrt{\bar{u}^2 + \bar{v}^2} \left(\frac{k}{b \ln\left(\frac{hf}{z_0}\right)} \right)^2 \right] \quad (22)$$

$$\frac{\partial \bar{v}}{\partial t} + \frac{\partial}{\partial y}(\bar{v}^2) + \frac{\partial}{\partial x}(\bar{u}\bar{v}) = -\frac{1}{\rho} \left[\Delta\rho g \frac{\partial H}{\partial y} + \rho\bar{v}\sqrt{\bar{u}^2 + \bar{v}^2} \left(\frac{k}{b \ln\left(\frac{hf}{z_0}\right)} \right)^2 \right] \quad (23)$$

In order to store the mesh variables h , \bar{u} and \bar{v} a staggered grid scheme was used. In this scheme the height of the flow, h , is stored in the centre of the grid cell. The components \bar{u} of the velocity in the x-direction are stored at the left and right faces of the grid cells, at a distance of $\pm \Delta x/2$ from the centre, and the \bar{v} components of the velocity in the y-direction are stored at the top and bottom of the grid cell, at a distance of $\pm \Delta y/2$ of the center.

On a staggered grid the scalar variables (pressure, density, total enthalpy, etc) are stored in the cell centres of the control volumes, whereas the velocity or momentum variables are located at the cell faces. This is different from a collocated grid arrangement, where all variables are stored in the same positions. A staggered storage is mainly used on structured grids for incompressible flow simulations. Using a staggered grid is a simple way to avoid odd-even decoupling between the pressure and velocity. Odd-even decoupling is a discretization error that can occur on collocated grids and which leads to checkerboard patterns in the solutions (CFD Online, Harlow & Welch, 1965).

Figure 1 shows a part of the computational domain discretized with staggered grid

scheme. The momentum equation in the x -direction, Eq. (22), is discretized at the position $i + 1/2, j$. Analogously, the momentum equation in the y -direction, Eq. (23), is discretized at the position $i, j + 1/2$. Lastly, the continuity equation, Eq. (21), is discretized at the point i, j located at the centre of the grid cell.

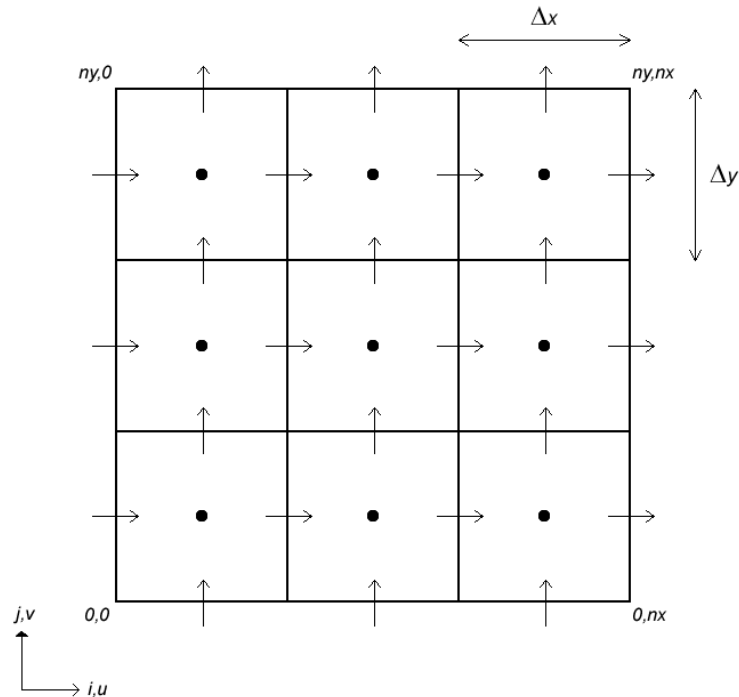


Figure 1: Staggered grid scheme. The height is stored at the centre of the grid and the components of velocity are stored at the left, right, top and bottom of the grid cell.

Consider the momentum equation in the x -direction discretization at the finite differences cell, Figure 2.

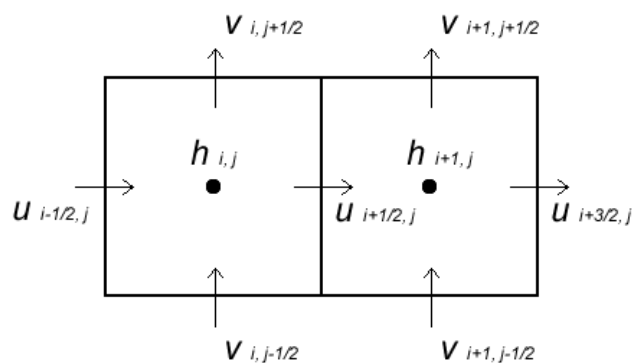


Figure 2: Discretization of the momentum equation in x -direction.

The discretization at the point $i + 1/2, j$ for the advection and pressure terms are done using second order central difference.

$$\frac{\partial H}{\partial x} \Big|_{i+1/2,j} \approx \frac{H_{i+1,j} - H_{i,j}}{\Delta x} \tag{24}$$

$$\frac{\partial}{\partial x} (\bar{u}^2) \Big|_{i+1/2,j} \approx \frac{\bar{u}^2_{i+1,j} - \bar{u}^2_{i,j}}{\Delta x} \tag{25}$$

$$\frac{\partial}{\partial y} (\bar{uv}) \Big|_{i+1/2,j} \approx \frac{(\bar{uv})_{i+1/2,j+1/2} - (\bar{uv})_{i+1/2,j-1/2}}{\Delta y} \tag{26}$$

The terms $\bar{u}^2_{i+1,j}$, $\bar{u}^2_{i,j}$, $(\bar{uv})_{i+1/2,j+1/2}$ and $(\bar{uv})_{i+1/2,j-1/2}$ in Eq. (25) and (26) are not defined on the grid, and are obtained by linear interpolation of the values of \bar{u} and \bar{v} located at the cell faces. The value of H in Eq. (24) is given by the sum of the deposit thickness, d , the z coordinate of the surface and the flow thickness, h .

The values of the velocity \bar{v} and the flow thickness h also are not defined at the point $i + 1/2, j$ in the last term of the Eq. (22). Then, the velocity \bar{v} at this point is given by the average of the velocities \bar{v} at the adjacent cell faces.

$$\bar{v} \Big|_{i+1/2,j} \approx \frac{\bar{v}_{i,j-1/2} + \bar{v}_{i+1,j-1/2} + \bar{v}_{i,j+1/2} + \bar{v}_{i+1,j+1/2}}{4} \tag{27}$$

Finally, the value of the flow thickness h at the point $i + 1/2, j$ is obtained by the average of the values located at the centre of the adjacent cell.

$$h \Big|_{i+1/2,j} \approx \frac{h_{i+1,j} + h_{i,j}}{2} \tag{28}$$

Analogously, the discretization of the momentum equation in y -direction, Eq. (23), at the point $i, j + 1/2$ is given according to the points showed in the Figure 3.

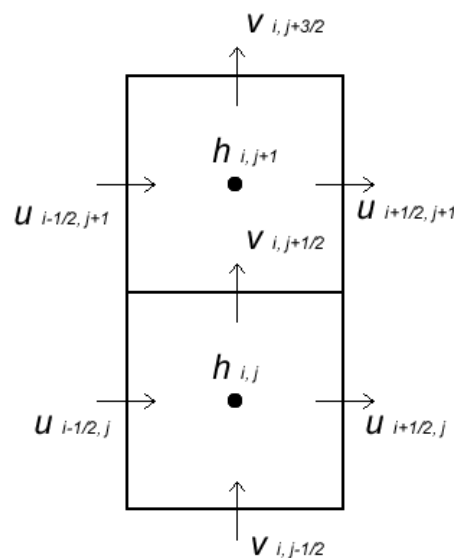


Figure 3: Discretization of the momentum equation in y -direction.

As mentioned before for the momentum equation in x-direction, the terms $\bar{v}^2_{i,j+1}$, $\bar{v}^2_{i,j}$, $(\bar{u}\bar{v})_{i+1/2,j+1/2}$ and $(\bar{u}\bar{v})_{i-1/2,j+1/2}$ in Eq. (30) and (31) are also not defined on the grid, and are obtained by linear interpolation of the values of \bar{u} and \bar{v} located at the cell faces.

$$\left. \frac{\partial H}{\partial y} \right|_{i,j+1/2} \approx \frac{H_{i,j+1} - H_{i,j}}{\Delta y} \quad (29)$$

$$\left. \frac{\partial}{\partial y} (\bar{v}^2) \right|_{i,j+1/2} \approx \frac{\bar{v}^2_{i,j+1} - \bar{v}^2_{i,j}}{\Delta y} \quad (30)$$

$$\left. \frac{\partial}{\partial x} (\bar{u}\bar{v}) \right|_{i,j+1/2} \approx \frac{(\bar{u}\bar{v})_{i+1/2,j+1/2} - (\bar{u}\bar{v})_{i-1/2,j+1/2}}{\Delta x} \quad (31)$$

The value of H in Eq. (29) is given by the sum of the deposit thickness, d , the z coordinate of the surface and the flow thickness, h . The average of velocity \bar{u} , Eq. (23), is given by the average of the velocities at the adjacent cell faces.

$$\bar{u}|_{i,j+1/2} \approx \frac{\bar{u}_{i-1/2,j} + \bar{u}_{i+1,j} + \bar{u}_{i-1/2,j+1} + \bar{u}_{i+1/2,j+1}}{4} \quad (32)$$

The flow thickness, h , is obtained by the average of the adjacent centre of the cells grids. See Eq. (33).

$$h|_{i,j+1/2} \approx \frac{h_{i,j+1} + h_{i,j}}{2} \quad (33)$$

The continuity equation, Eq. (21), is calculated using upwind scheme. Upwind schemes use an solution-sensitive finite difference stencil to numerically simulate more properly the direction of propagation of information in a flow field. The upwind schemes attempt to discretize hyperbolic partial differential equations by using differencing biased in the direction determined by the sign of the characteristic speeds (Wikipedia, Patankar, 1980). For example, at the point i,j the continuity equation discretization is given according to the points showed in the Figure 4.

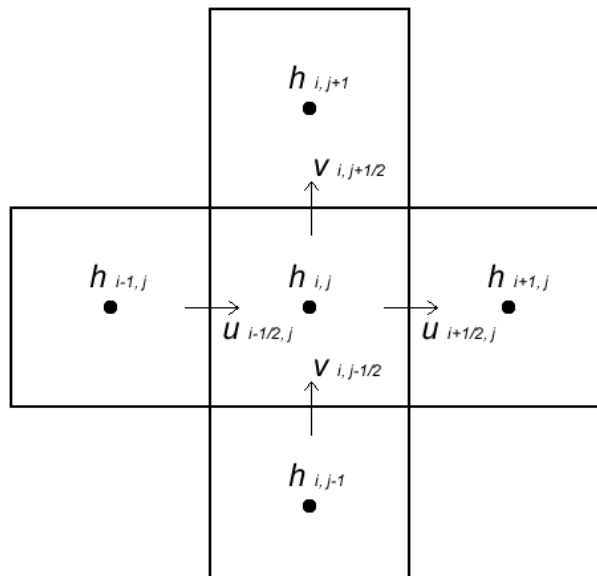


Figure 4: Discretization of the continuity equation derivatives.

The first RHS term of the Eq. (21), which represents the derivative of the function with respect to x , is given by:

$$\frac{\partial}{\partial x}(h\bar{u})\Big|_{i,j} \approx \frac{h_d\bar{u} - h_e\bar{u}}{\Delta x} \tag{34}$$

where:

$$h_d = \begin{cases} h_{i,j}, & \bar{u}_{i-1/2,j} < 0 \\ h_{i-1,j}, & \bar{u}_{i-1/2,j} \geq 0 \end{cases} \tag{35}$$

$$h_e = \begin{cases} h_{i+1,j}, & \bar{u}_{i+1/2,j} < 0 \\ h_{i,j}, & \bar{u}_{i+1/2,j} \geq 0 \end{cases} \tag{36}$$

And the second RHS term, which represents the derivative of the function with respect to y , is given by:

$$\frac{\partial}{\partial y}(h\bar{v})\Big|_{i,j} \approx \frac{h_t\bar{v} - h_b\bar{v}}{\Delta y} \tag{37}$$

where:

$$h_t = \begin{cases} h_{i,j+1}, & \bar{v}_{i,j+1/2} < 0 \\ h_{i,j}, & \bar{v}_{i,j+1/2} \geq 0 \end{cases} \tag{38}$$

$$h_b = \begin{cases} h_{i,j}, & \bar{v}_{i,j-1/2} < 0 \\ h_{i,j-1}, & \bar{v}_{i,j-1/2} \geq 0 \end{cases} \tag{39}$$

The time discretization of the momentum equations is based on the explicit Euler method, where all terms involving the velocity are discretized in time n . Then the

term involving the flow thickness h is discretized in time $n + 1$. Thus, after the calculation of the velocities \bar{u}^{n+1} and v^{n+1} , all the variables have been advanced in time.

The equations are easily calculated in time n using explicit methods. However, these methods present some stability restrictions, which limit the range of values that can be used for the Δt . On the other hand, implicit discretizations provide a set of equations which must be solved together thereby consuming more processing power to solve them. Therefore, the time discretization of the continuity equation, Eq. (21), at the point i, j of the grid cell is given by:

$$\frac{h_{i,j}^{n+1} - h_{i,j}^n}{\Delta t} \approx - \left(\frac{h_d \bar{u} - h_e \bar{u}}{\Delta x} + \frac{h_t \bar{v} - h_b \bar{v}}{\Delta y} \right) - \frac{s_k}{c_k} \quad (40)$$

The time discretization of the momentum equations in the directions of x and y at the face of the grid cell i, j , are obtained by the Eq. (41) and (42), respectively.

$$\begin{aligned} \frac{\bar{u}_{i+1/2,j}^{n+1} - \bar{u}_{i+1/2,j}^n}{\Delta t} & \approx - \frac{\Delta \rho g H_{i+1,j} - H_{i,j}}{\rho \Delta x} \\ & - \left(\frac{\bar{u}_{i+1,j}^2 - \bar{u}_{i,j}^2}{\Delta x} + \frac{(\bar{u}\bar{v})_{i+1/2,j+1/2} - (\bar{u}\bar{v})_{i+1/2,j-1/2}}{\Delta y} \right) \\ & - \bar{u}_{i+1/2,j}^n \sqrt{(\bar{u}_{i+1/2,j}^n)^2 + (\bar{v}_{i+1/2,j}^n)^2} \left(\frac{k}{b \ln \left(\frac{h_{i+1/2,j} f}{z_0} \right)} \right)^2 \end{aligned} \quad (41)$$

$$\begin{aligned} \frac{\bar{v}_{i,j+1/2}^{n+1} - \bar{v}_{i,j+1/2}^n}{\Delta t} & \approx \frac{\Delta \rho g H_{i,j+1} - H_{i,j}}{\rho \Delta y} \\ & - \left(\frac{\bar{v}_{i,j+1}^2 - \bar{v}_{i,j}^2}{\Delta y} + \frac{(\bar{u}\bar{v})_{i+1/2,j+1/2} - (\bar{u}\bar{v})_{i-1/2,j+1/2}}{\Delta x} \right) \\ & - \bar{v}_{i,j+1/2}^n \sqrt{(\bar{u}_{i,j+1/2}^n)^2 + (\bar{v}_{i,j+1/2}^n)^2} \left(\frac{k}{b \ln \left(\frac{h_{i,j+1/2} f}{z_0} \right)} \right)^2 \end{aligned} \quad (42)$$

3.2 Stability

The numerical method stability is obtained using the Courant-Friedreichts-Lewy condition, also known as CFL condition. This condition represents the relation between the size of the grid cell, the time step and the inflow velocity, and it ensures the solution stability of the explicit methods.

This condition declares that the numeric wave should propagate as fast as the

physic wave, which means that the numeric wave velocity $\Delta x/\Delta t$ must be at least as fast as the physic wave velocity $|u|$, i.e. $\Delta x/\Delta t > |u|$ (Osher & Fedkiw, 2002). Thus, the CFL condition can be written as

$$\Delta t < \frac{\Delta x}{\max\{|u|\}} \quad (43)$$

The term $\max\{|u|\}$ is given by the maximum value of the grid velocity. The Eq. (43) is usually applied assuming a general number for the CFL constant.

$$\Delta t \left(\frac{\max\{|u|\}}{\Delta x} \right) = \alpha \quad (44)$$

where $0 < \alpha < 1$. According to Osher & Fedkiw (2002), a good choice is $\alpha = 0.9$ or a more conservative choice of $\alpha = 0.5$. The CFL condition can also be written as

$$\Delta t \left(\frac{\max\{|\vec{V}|\}}{\min\{\Delta x, \Delta y, \Delta z\}} \right) = \alpha \quad (45)$$

4 OVERVIEW OF THE SOFTWARE

All presented equations were implemented into the software program, Turb3D. It can be used to simulate the evolution and deposition of low density turbidity currents using multi grain-sizes. This application has a user-friendly GUI for data entry and result visualizations, Figure 5.

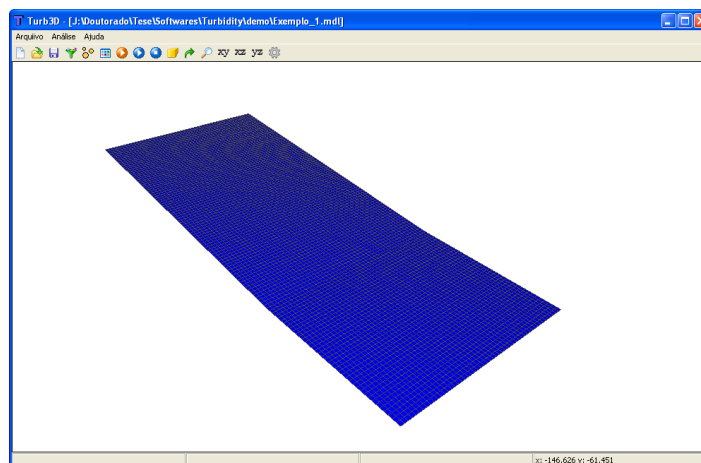


Figure 5: Turb3D application.

Turb3D require some inputs in order to start a new simulation. The first step is to define an initial surface. It can be done by pressing the "new" button located at the toolbar of the application. A new project dialog will then be showed, see Figure 6. In this dialog a file containing the x,y,z coordinates of the surface is imported. This file consists of three columns of data. The first column represents the x coordinate of the surface, the second represents the y coordinate and the third represents de z coordinate. The size, length and width of the grid are calculated automatically by the

program based on the coordinates information which are read from file.

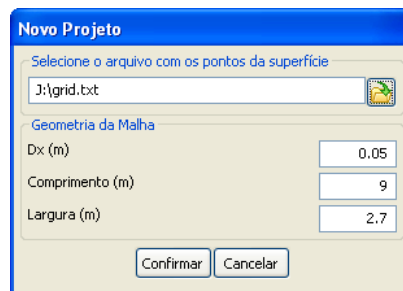


Figure 6: New project dialog.

Then, it is necessary to define the inflow channel by pressing the “channel” button, Figure 7. In this dialog the height of the channel is specified along with two points representing its initial and final coordinates.

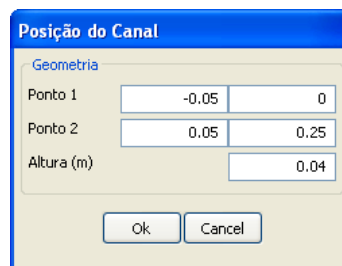


Figure 7: Channel dialog.

The current parameters are specified by pressing the “current” button. Then, the current dialog will be displayed as shown in Figure 8.

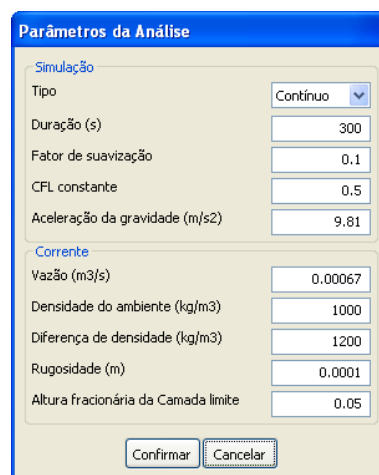


Figure 8: Current dialog.

Finally, the sediment parameter is specified as shown in Figure 9. For each grain size it is necessary to specify the diameter of the grain and the concentration of the grain in the current. For additional information the grain distribution graph is plotted.

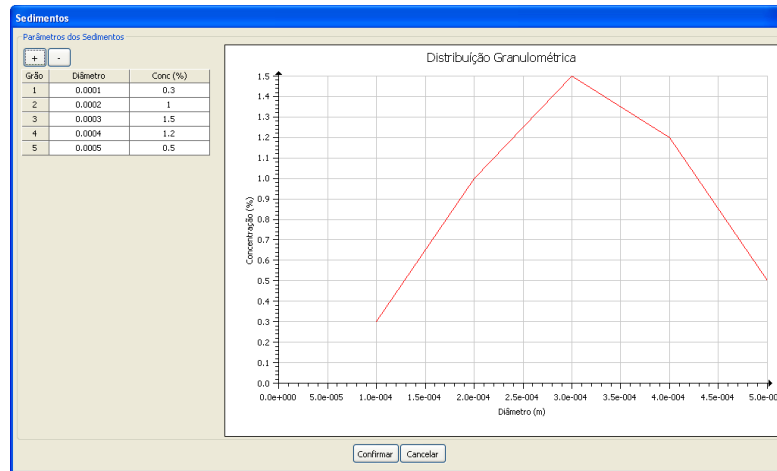


Figure 9: Sediment dialog.

After these steps, the simulation can be processed by pressing the “run” button. The evolution and deposition of the simulation are rendered in real-time.

4.1 Examples

The numerical model proposed must be validated by experiments in order to check if the simplifications and assumptions used by this work are valid. In other words, it is fundamental to verify whether the results obtained by using the application can produce a good prediction of the evolution and deposition of the current. Then, two examples of experiments that can be performed in laboratories are simulated using Turb3D.

Simulations are ran using single-grain-size suspensions at 100 and 150 microns with concentration of 2% by volume, grain density of 2600 kg/m^3 and a 40 l/min inflow. The initial surface file used was created considering a tank with dimensions of 10 m in length, 5 m in width and a 4 degree slope, which generates a file containing 55 nodes in x-direction and 181 nodes in y-direction for a grid size of 0.05 m. The CFL constant used was 0.5.

Figure 10 shows the 3D contour plot of the surface deposit generated by the simulation using single-grain-size at 100 microns. The red colour represents the maximum values and the blue colour represents the minimum values. For this example the maximum deposit thickness archived was 26.60 mm.

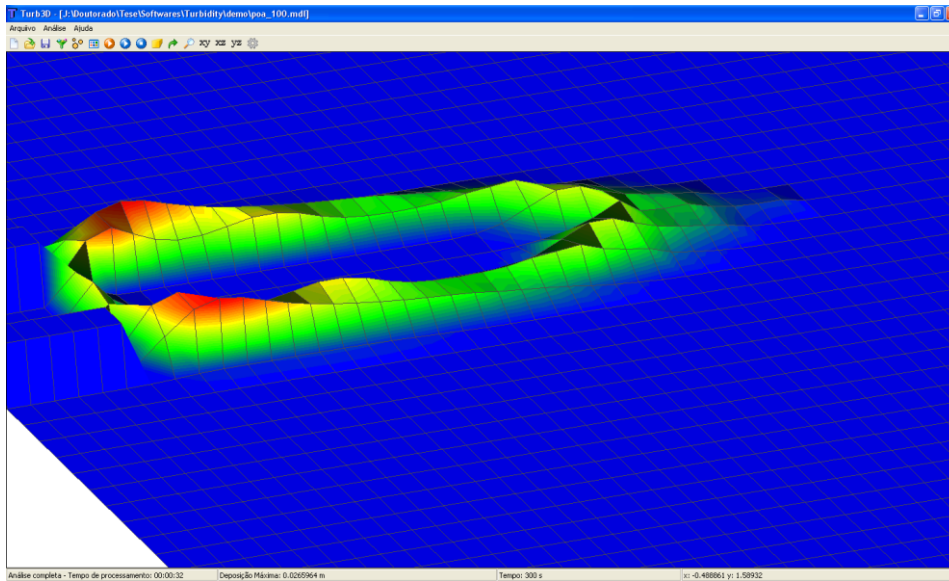


Figure 10: Single-grain-size at 100 microns simulation.

The 3D contour plot of the surface deposit generated by the simulation using single-grain-size at 150 microns is shown in Figure 11. Again, the red colour represents the maximum values and the blue colour represents the minimum values. For this example the maximum deposit thickness archived was 55.90 mm.

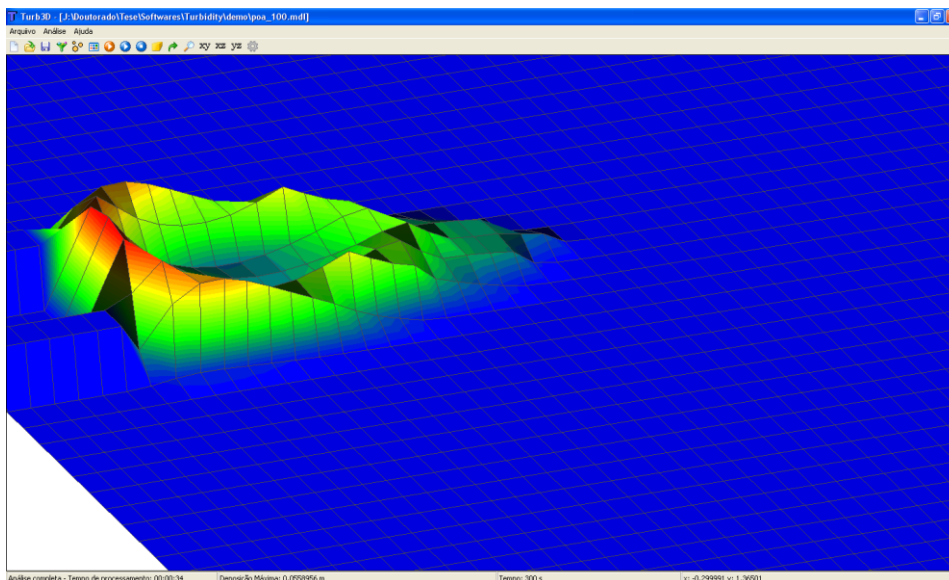


Figure 11: Single-grain-size at 150 microns simulation.

5 CONCLUSIONS

The main objectives of this work are to propose a consistent numerical model for making predictions of the sedimentation processes in stratigraphic modelling which requires less CPU resources, and to develop a 3D graphical application for turbidity currents simulation. Furthermore, its important to note that the proposed numerical

method concentrates only on the simulation of the depositional process and not on the complete turbulent flow.

The numerical model proposed was satisfactory in terms of computational resources, it was faster than complex models which can consume days of continuous processing power to solve a single model. The examples presented were ran on a computer with a 2.50GHz core duo processor and 2GB of RAM. Each example took about 35 seconds to complete the simulation process.

Despite the good computational performance achieved by using this approach, experiments should be done in order to validate the proposed numerical method presented in this work.

REFERENCES

- Abramowitz, M. & Stegun, I.A. *Handbook of Mathematical Functions*. Dover Publications, 1965.
- Acheson, D.J. *Elementary Fluid Mechanics*. Clarendon Press, 1990.
- Allen, P.A. *Earth Surface Processes*. Blackwell Science, 1997.
- Bagnold, R.A. An approach to the sediment transport problem from general physics. Professional Paper, 422. *US Geological Survey*, Washington. 1966.
- Bitton, L.F.; Martha, L.F.; Waltham, D.; Keevil, G.; Peakall, J. Validation of Simplified Mathematical Model for Turbidity Currents. *SPE Annual Technical Conference and Exhibition*, 21–24 September 2008, Denver, Colorado, USA. 2007.
- CFD Online Available at: www.cfd-online.com (Accessed 24 August 2008)
- Duncan, W.J., Thom, A.S.; Young, A.D. *The Mechanics of Fluids*. Edward Arnold, London. 1960.
- Harlow, F.H. and Welch, J.E. Numerical calculation of time-dependent viscous incompressible flow of fluid with free surface. *Phys. Fluids*. 8, 2182, 1965
- Kneller, B., Bennett, S.; McCaffrey, W. Velocity structure, turbulence and fluid stresses in experimental gravity currents. *Journal of Geophysical Research*, C104, 5381–5391, 1999.
- Leeder, M.R., Gray, T.E.; Alexander, J. Sediment suspension dynamics and a new criterion for the maintenance of turbulent suspensions. *Sedimentology*, 52, 683–691, 2005.
- Osher, S.J.; Fedkiw, R. *Level Set Methods and Dynamic Implicit Surfaces*. SpringerVerlag, 2002.
- Patankar, S.V. *Numerical Heat Transfer and Fluid Flow*. Taylor & Francis, 1980
- Raudkivi, A. *Loose Boundary Hydraulics*. Balkema, Rotterdam. 1998.
- Rouse, H. Modern conceptions of the mechanics of turbulence. *Transaction of the American Society of Civil Engineers*, 102, 436–505, 1937.
- Waltham, D. Flow transformations in particulate gravity currents. *Journal of Sedimentary Research*, 74(1), 129-134, 2004.
- Wikipedia, the free encyclopedia Available at: www.wikipedia.org (Accessed 2 June 2008)